Performance Simulation of SmallSat SAR Persistent Scatterer Interferometry with Deteriorated Images

Jan Krecke, Oliver Kim, Michelangelo Villano *Senior Member, IEEE,*
Gerhard Krieger *Fellow, IEEE,* Mohammed Dabboor *Senior Member, IEEE,*
John E. Cater *Member, IEEE*, and Andrew C. M. Austin *Member, IEEE*

Abstract—The performance trade-offs required for a small satellite Synthetic Aperture Radar (SAR) system designed to measure surface deformations using persistent scatterer interferometry (PSI) are investigated. Existing X-band satellite data is systematically deteriorated to account for the increased range resolution and Noise-Equivalent Sigma Zero (NESZ). It is found that with a NESZ below $0\,\mathrm{dB}$ the deformation signal of a selected region-of-interest (ROI) can be captured with mean absolute errors of $5\,\mathrm{mm}$ and $15\,\mathrm{mm}$, for ground range resolutions of $5\,\mathrm{m}$ and $20\,\mathrm{m}$ respectively. This analysis is used to develop preliminary SAR system designs suitable for small satellites.

Index Terms—Sensing Platforms, Processing, Sensors and Systems for SAR Data.

I. INTRODUCTION

SATELLITE data have been successfully used for mapping the Earth's topography since the early days of Synthetic Aperture Radar (SAR) [1], [2], and Interferometric SAR (InSAR) time-series techniques have been used for more than 20 years to measure surface deformations [3]. An early type of InSAR that uses the scattering properties of a discrete set of persistent reflectors, persistent scatterer interferometry (PSI), was first proposed in 2001 [4], and different algorithms, and implementations have been proposed ever since [5].

PSI is an attractive solution to the problem of determining movement as it allows for the mapping of wide swathes of the Earth's surface, so that large deformation phenomena can be more easily characterised than with the conventional Continuous Global Navigation Satellite System (CGNSS) approach using fixed ground stations. The disadvantage of the PSI approach is the reduced temporal resolution. This could be mitigated by employing multiple small SAR satellites (in a constellation) to increase the revisit frequency for each spot on the ground.

The goal of this work is to determine whether a purpose-built small-satellite SAR system could yield large-scale deformation maps using PSI with acceptable accuracy. The quality of the images produced by this system will likely be significantly lower than that of conventional multi-purpose SAR systems such as TerraSAR-X (TS-X). However, it is anticipated that the associated system design can be simpler

J. Krecke and O. Kim are with the University of Auckland, Auckland, New Zealand; M. Villano and G. Krieger are with the German Aerospace Centre, Oberpfaffenhofen, Germany; M. Dabboor is with the Department of Environment and Climate Change Canada, Ottawa, Canada; J.E. Cater is with the University of Canterbury, Christchurch, New Zealand; and A.C.M. Austin is with the University of Bristol, Bristol, UK.

and less expensive. Similar findings resulted from the design of a system for ship detection using a CubeSat platform [6], [7]. Accordingly, this work identifies the minimum SAR image quality requirements necessary for a PSI algorithm to identify deformation phenomena. To achieve this, a TS-X data set is modified by changing the noise level and range resolution as a deterioration in these two properties is typically associated with small-satellite SAR systems [8].

II. METHODOLOGY

To estimate the parameter values required for the minimum SAR image quality, two approaches are possible: an analytical approach and a simulation-based approach. For the analytical approach, the expected PSI performance for a given parameter set could be derived from first principles. This is challenging as the outcome depends upon a large number of factors, including orbit errors, atmospheric errors and look-angle errors [9]. Another difficulty is that different PSI algorithms use different persistent scatterer (PS) selection criteria, which means that the number and quality of scatterers cannot be predicted without considering a specific algorithm.

The alternative approach developed in this work uses simulations to deteriorate an existing SAR data set in systematic ways and applies a widely-used PSI processing chain. The PSI deformation map obtained for the deteriorated data set is then compared to a baseline deformation map obtained from the original data. This procedure can be used for multiple parameter combinations, and by computing the root-mean-square error (RMSE) for each, the separate influence of different factors can be empirically determined.

This investigation uses the Stanford Method for Persistent Scatterers (StaMPS) algorithm [10]. StaMPS was chosen because it is implemented as a Free-and-Open-Source-Software (FOSS) tool [11] that has been successfully used to characterise large scale deformation phenomena [12], [13]. The SAR data are sourced from the TS-X mission [14], which together with its twin satellite TanDEM-X, has been designed with the application of InSAR in mind [15].

For the proposed small satellite SAR system, the space for solar panels and on-board energy storage is limited, and hence the transmit power will be low when compared to conventional systems. This in turn negatively affects the thermal noise level present in the images. The range resolution is also an important factor in this analysis as it is inversely proportional to the radar chirp bandwidth, and the chirp bandwidth is
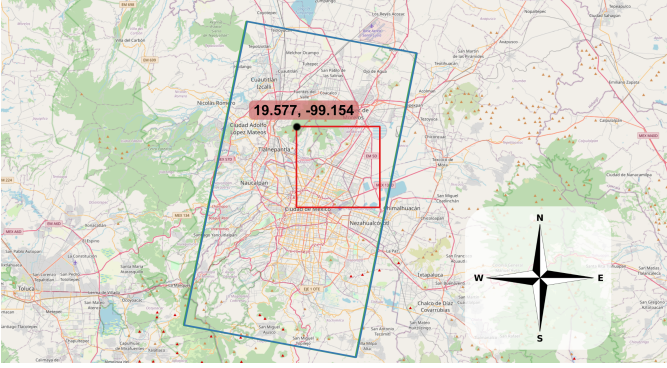
Fig. 1. Footprint of the TS-X beam (blue) covering Mexico City, and the ROI used for PSI processing (red). The top left corner of the ROI is $(19.577, -99.154)$.
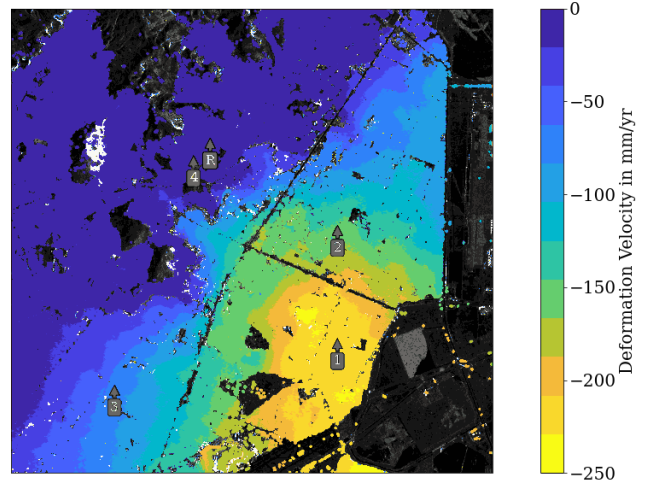

Fig. 2. Baseline persistent scatterer interferometry deformation map. The PS locations are overlaid on the intensity SAR image of the master scene, colored by mean velocity.

directly proportional to the thermal noise power. Hence, the requirements for range resolution and noise level must be balanced. The azimuth resolution is left unchanged from the baseline data for this analysis as it is already achievable for a small satellite antenna [6]–[8].

A. Baseline Data

Mexico City has been selected as a test region, as the subsidence phenomena in the area have been well characterised by both land-based measurements and InSAR studies [16]–[19]. The city is built on an aquifer, which compresses due to the extraction of groundwater [20], and this causes significant deformation over time in some areas. The ground footprint of the TS-X beam and the region-of-interest (ROI) used for the PSI processing are shown in Fig. 1.

The selected ROI includes Mexico City airport in the South, and a forested mountainous area in the North. This section was chosen as it includes zones of both small deformation and large subsidence. The extent of the ROI is $15.8\,\mathrm{km}$ in the East-West direction, and $16.3\,\mathrm{km}$ in the North-South direction.

The SAR data set consists of a stack of 30 TS-X stripmap Single-Look Slant range Complex (SSC) images acquired over a period of 30 months between October 2017 and March 2020. TS-X data were chosen because they are acquired in X-band, which is the most likely choice for a dedicated small-satellite SAR mission [6]. The nominal resolution of the data in azimuth is $3.3\,\mathrm{m}$ and $2.3\,\mathrm{m}$ in range (although the precise resolution varies with the angle of incidence). The data have HH-polarization and were recorded during a descending orbit.

B. Processing Workflow

To determine how the PSI algorithm performs on data of varying image quality, the baseline data set is systematically deteriorated in Noise-Equivalent Sigma Zero (NESZ) and range resolution. After the data are modified, the PSI algorithm is applied.

Complex Gaussian noise is initially added to the SSC data to deteriorate the TS-X data for different levels of NESZ, e.g.,

$$u_{\mathrm{noisy}} = u_0 + n_{\mathrm{cal}}, \qquad (1)$$

where u_0 are the original SAR data, u_{noisy} are the modified data and n_{cal} is complex Gaussian noise, processed using the appropriate calibration look-up table (LUT) to ensure that the noise power corresponds to the desired NESZ value.

The deterioration of the range resolution is achieved by truncating the spatial spectrum of the SAR data in proportion to the desired reduction in range resolution. For ease of implementation, the number of image pixels is not changed as the spatial bandwidth is reduced. Initial interferometric pre-processing is conducted using the snap2stamps workflow [21]. The surface deformation pattern and the PSI time series of the ROI are then determined using the StaMPS MATLAB tool [22]. After the PSI processing, the PS deformation values are interpolated onto a common grid to enable comparison.

The ROI is filled with a grid of 141×141 interpolation points, which corresponds to a grid spacing of $112.1\,\mathrm{m}$ in the East-West direction, and $115.6\,\mathrm{m}$ in the North-South direction. Only grid points that are surrounded by at least two persistent scatterers within a radius of $100\,\mathrm{m}$ are used for the interpolation. The interpolation of the PS deformation values onto the grid points uses a 2D linear interpolator [23], [24].

An error can be computed with reference to the baseline data. The selected measure is the mean absolute error (MAE), which is defined as

$$\mathrm{MAE} = \frac{1}{M_{\mathrm{grid}} N_{\mathrm{ifg}}} \sum_{i=0}^{M_{\mathrm{grid}}-1} \sum_{j=0}^{N_{\mathrm{ifg}}-1} |d_{\mathrm{bl},i,j} - d_{\mathrm{noise},i,j}|, \qquad (2)$$

where M_{grid} is the number of grid points used for the interpolation of the deformation map, N_{ifg} is the number of interferograms used to generate the time series, and $d_{\mathrm{bl},i}$ and $d_{\mathrm{noise},i}$ represent the interpolated deformation results for the baseline data set and the noisy data set, respectively. The MAE is computed for each time series (represented by the index j). The MAEs for all PS time series are averaged over all PS locations (represented by the index i). In this way, a single error measure for each noise level is computed.
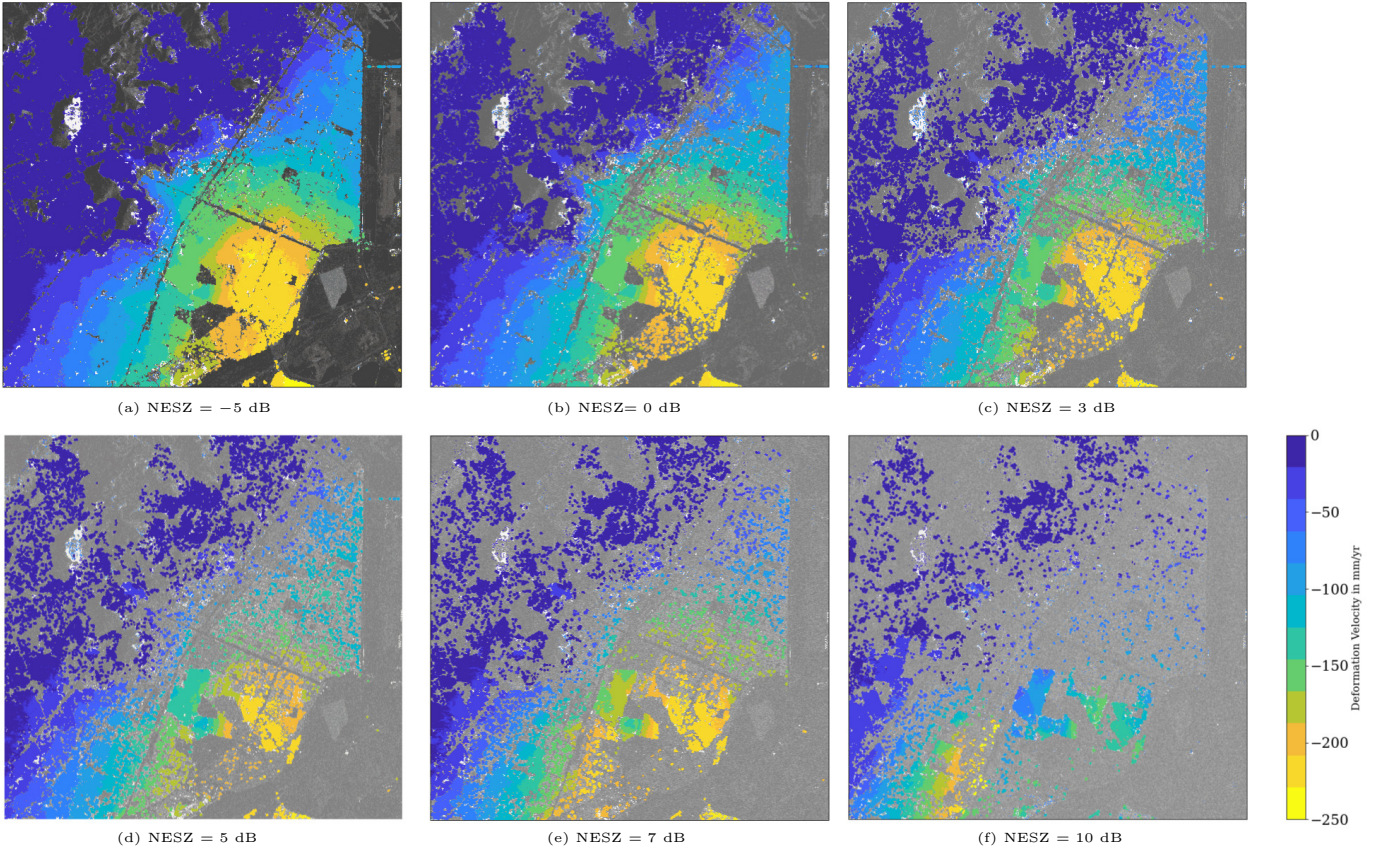
Fig. 3. PSI deformation maps for different NESZ levels. The legend is the same for all sub-figures.

III. PSI RESULTS

A. Baseline Results

The deformation velocities for all persistent scatterers in the data set described in Sec. II-A are shown in Fig. 2. The figure shows that the density of persistent scatterers is relatively high in most of the ROI. Only forested and desert areas do not contain any structures recognised by the StaMPS algorithm. It is observed that significant roads in densely populated areas of the ROI are also free of persistent scatterers. The deformation map confirms that Mexico City is subject to strong subsidence in the central south-eastern part of the ROI. From there, the mean deformation velocity decreases in a semi-circular pattern. At the city's fringes, the subsidence is nearly zero; these observations agree with those in previous work [18].

B. Noise Analysis

Fig. 3 shows the deformation maps obtained for different NESZ values. It is observed that the PS density decreases with increasing noise. This is because a higher noise level deteriorates the phase stability of each pixel. Hence, as the noise increases, fewer pixels fulfil the StaMPS phase stability criteria. The data show that the ability to capture the spatial characteristics of the deformation pattern is maintained up to a noise level of approximately NESZ $= 5$ dB, as clusters of PS are formed in many areas of the ROI. Thus, although the overall PS density decreases rapidly, the spatial distribution

of the remaining scatterers remains similar even for relatively high noise values.

The ability to capture the deformation pattern observed in the baseline data set at higher noise levels is characterised by the MAE. Given that adding noise to SAR images is an inherently statistical process, the MAE of the StaMPS processing for any given noise level may be subject to statistical variations. Therefore, more robust estimates can be obtained by averaging the MAE values obtained for multiple noise realisations. This is computationally expensive, so in this work a compromise was made to evaluate the average MAE from five different noise realisations per NESZ value.

C. Resolution Analysis

The resolution of the system in range is given by

$$\Delta R_{\mathrm{g}} = \frac{c}{2B_r \sin \eta}, \tag{3}$$

which depends on the bandwidth of the radar pulse B_r and the angle of incidence at the ground η. The constant c is the speed of light.

To investigate the influence of the NESZ and range resolution on the MAE, a joint parameter analysis was conducted for different combinations. The results of this analysis are shown in Fig. 4, which was obtained by simulating 20 equally spaced points in the NESZ-ΔR_{g}, similar to [6]. As expected, increasing NESZ and ΔR_g increases the MAE. However, this
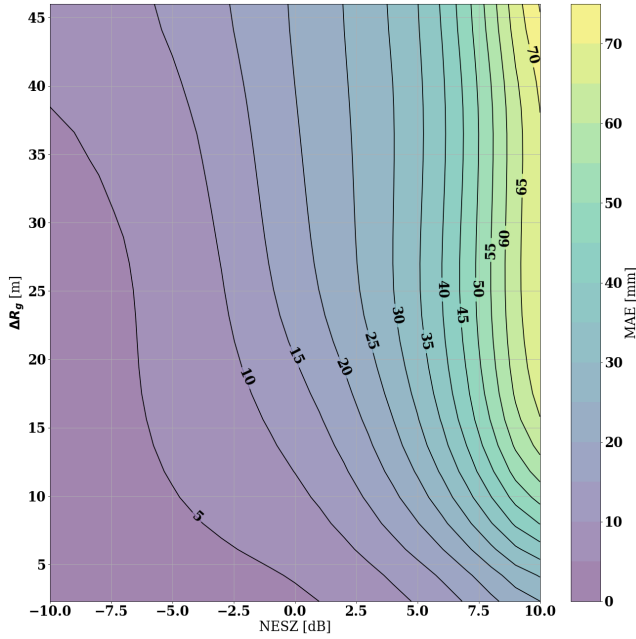
Fig. 4. Contours of constant deformation MAE (in mm) as a function of NESZ (dB) and range resolution ΔR_g (m).
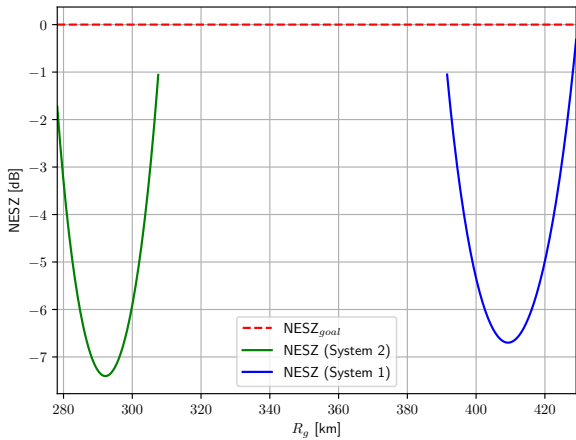

Fig. 5. NESZ versus ground range for the system parameters shown in Tab. I showing NESZ within the $3\,\mathrm{dB}$ beamwidth of the antenna beam on ground.

behaviour is not linear, and depending on the specific zone of operation, there is variable sensitivity to the degraded inputs. In particular, for values of ΔR_g greater than approximately $20\,\mathrm{m}$ the MAE is largely determined by the NESZ.

IV. PRELIMINARY SYSTEM DESIGN

The contour lines of constant MAE in Fig. 4 identify possible system designs that trade-off NESZ and range resolution ΔR_g. A number of operating points are possible, and two alternatives are compared here: System 1 (S1) is optimised for an MAE of $5\,\mathrm{mm}$, and System 2 (S2) is optimised for an MAE of $15\,\mathrm{mm}$. For an NESZ of 0 dB (considered feasible for a small-satellite platform [6], [8]), these systems correspond to ground range resolutions of approximately 5 m and 20 m

TABLE I
SYSTEM DESIGN PARAMETERS

Parameter	Symbol	Value	Units
Average transmit power	P_{avg}	15 (S1) & 1.5 (S2)	W
Wavelength	λ	0.03	m
Antenna length	L_{a}	4	m
Antenna width	W_{a}	0.71	m
Antenna gain	G	46	dB
Look angle	γ	38.6 (S1) & 30 (S2)	°
Orbit height	H	500	km
Satellite velocity	v	7100	$\mathrm{m\,s^{-1}}$
Noise temperature	T_{s}	300	K
Noise figure	F	5	dB
System losses	L	5	dB
Rx bandwidth	B_{r}	100 (S1) & 15 (S2)	MHz

respectively. All other parameters for the proposed system designs are shown in Tab. I [25].

The SAR radar equation for a distributed target is [25]

$$\mathrm{NESZ} = \frac{256\pi^3 r^3 B_{\mathrm{r}} \sin\theta_{\mathrm{i}} v k T_{\mathrm{s}} F L}{P_{\mathrm{avg}}\, G^2\, \lambda^3\, c}\,, \qquad (4)$$

where θ_{i} the angle of incidence, and r is the slant range from the satellite to ground. The receiver bandwidths for the two designs are 100 MHz (S1) and 15 MHz (S2) respectively. Fig. 5 shows the NESZ computed for both designs as a function of the ground range (determined using a spherical earth model), using the parameters in Tab. I.

The parameters shown in Tab. I reflect the smallest possible platform. Even though the system power of 15 W is lower than that of existing conventional SAR missions, a swath width of $32.75\,\mathrm{km}$ can be achieved. In addition, an NESZ of below $0\,\mathrm{dB}$ is achieved over the entire swath width. Hence, given the range resolution and NESZ estimates, the resulting deformation map corresponds to that shown in Fig. 3(b).

The parameters for System 1 were selected to yield a relatively high resolution at a reduced noise level. The average range resolution over the whole swath width is $2.24\,\mathrm{m}$, which is close to the $2.3\,\mathrm{m}$ range resolution of the baseline data set used for the study in Sec. III. In contrast, for System 2 the ground range resolution is significantly lower due to the reduced bandwidth and steeper incidence. The maximum acceptable NESZ remains at $0\,\mathrm{dB}$, which means that the average transmit power can be decreased by a factor of 10, to $1.5\,\mathrm{W}$, and still meet the requirements. The average range resolution achieved with System 2 is $18.6\,\mathrm{m}$, and the swath width is $26.3\,\mathrm{km}$.

The MAE between the deformation signal and the deformation map obtained with System 2 is less than $15\,\mathrm{mm}$. The deformation map obtained for this case is presented in Fig. 6, showing that whilst the number of persistent scatterers has decreased, the overall deformation pattern from Fig. 2 remains discernible. This result demonstrates that a system design optimised for an MAE of $15\,\mathrm{mm}$ could be sufficient to detect deformation patterns such as those in Mexico City. For interferometric applications related to distributed scatterers, different combinations of resolution and noise level of the SAR images may result in better performance.
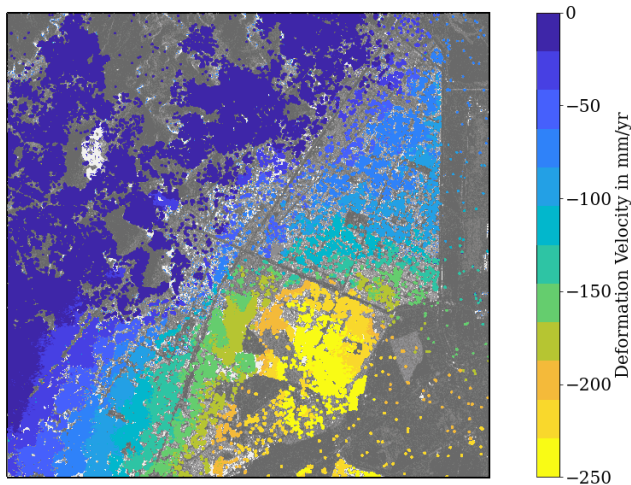
Fig. 6. PSI deformation map obtained for NESZ = 0 dB, ΔR_g = 20m. The resulting MAE is 15 mm.

This analysis is not only relevant for the design of a Small-Sat SAR systems, but also applies (in particular, the case of high-resolution/poor-NESZ) to recently proposed ambiguous SAR modes. These aim at mapping large swath with high resolution allowing for a high level of noise-like ambiguities (e.g., ambiguous staggered SAR mode), so far used for ship monitoring [7], [26], [27].

V. CONCLUSIONS

This work has presented the derivation of requirements for a small-satellite SAR system for the application of measuring surface deformations using PSI. These requirements were derived by analysing the performance of a PSI processing algorithm on SAR data of varying quality. In particular, a stack of 30 TS-X stripmap SAR images over Mexico City was modified by deteriorating the NESZ and the range resolution. It was found that the mean error in the deformation map depends on the NESZ and range resolution. For an NESZ below 0 dB, the deformation can be captured with mean absolute errors of 5 mm and 15 mm, for ground range resolutions of 5 m and 20 m respectively. A preliminary system design was derived from these constraints on the image quality, which is compatible with the objective of a small-satellite SAR system.

REFERENCES

[1] R. Bamler and P. Hartl, "Synthetic aperture radar interferometry," *Inverse problems*, vol. 14, no. 4, p. R1, 1998.

[2] P. A. Rosen, S. Hensley, I. R. Joughin, F. K. Li, S. N. Madsen, E. Rodriguez, and R. M. Goldstein, "Synthetic aperture radar interferometry," *Proceedings of the IEEE*, vol. 88, no. 3, pp. 333–382, 2000.

[3] D. Ho Tong Minh, R. Hanssen, F. Rocca *et al.*, "Radar interferometry: 20 years of development in time series techniques and future perspectives," *Remote Sensing*, vol. 12, no. 9, p. 1364, 2020.

[4] A. Ferretti, C. Prati, and F. Rocca, "Permanent scatterers in SAR interferometry," *IEEE Transactions on geoscience and remote sensing*, vol. 39, no. 1, pp. 8–20, 2001.

[5] M. Crosetto, O. Monserrat, M. Cuevas-González, N. Devanthéry, and B. Crippa, "Persistent scatterer interferometry: A review," *ISPRS Journal of Photogrammetry and Remote Sensing*, vol. 115, pp. 78–89, 2016.

[6] J. Krecke, M. Villano, N. Ustalli, A. C. M. Austin, J. E. Cater, and G. Krieger, "Detecting Ships in the New Zealand Exclusive Economic Zone: Requirements for a Dedicated SmallSat SAR Mission," *IEEE Journal of Selected Topics in Applied Earth Observations and Remote Sensing*, vol. 14, pp. 3162–3169, 2021.

[7] N. Ustalli, G. Krieger, and M. Villano, "A low-power, ambiguous synthetic aperture radar concept for continuous ship monitoring," *IEEE Journal of Selected Topics in Applied Earth Observations and Remote Sensing*, vol. 15, pp. 1244–1255, 2022.

[8] A. Freeman, "Design principles for smallsat SARs," in *32nd Annual AIAA/USU Conference on Small Satellites, 2018, Logan, UT*, 2018.

[9] A. Parizzi, R. Brcic, and F. De Zan, "InSAR performance for large-scale deformation measurement," *IEEE Transactions on Geoscience and Remote Sensing*, 2020.

[10] A. Hooper, P. Segall, and H. Zebker, "Persistent scatterer interferometric synthetic aperture radar for crustal deformation analysis, with application to volcán Alcedo, Galápagos," *Journal of Geophysical Research: Solid Earth*, vol. 112, no. B7, 2007.

[11] A. Hooper, D. Bekaert, K. Spaans, and M. Arıkan, "Recent advances in sar interferometry time series analysis for measuring crustal deformation," *Tectonophysics*, vol. 514, pp. 1–13, 2012.

[12] J. M. Delgado Blasco, M. Foumelis, C. Stewart, and A. Hooper, "Measuring urban subsidence in the Rome metropolitan area (Italy) with Sentinel-1 SNAP-StaMPS persistent scatterer interferometry," *Remote Sensing*, vol. 11, no. 2, p. 129, 2019.

[13] F. Cian, J. M. D. Blasco, and L. Carrera, "Sentinel-1 for monitoring land subsidence of coastal cities in Africa using PSInSAR: A methodology based on the integration of SNAP and staMPS," *Geosciences*, vol. 9, no. 3, p. 124, 2019.

[14] R. Werninghaus and S. Buckreuss, "The TerraSAR-X mission and system design," *IEEE Transactions on Geoscience and Remote Sensing*, vol. 48, no. 2, pp. 606–614, 2009.

[15] G. Krieger, A. Moreira, H. Fiedler, I. Hajnsek, M. Werner, M. Younis, and M. Zink, "TanDEM-X: A satellite formation for high-resolution SAR interferometry," *IEEE Transactions on Geoscience and Remote Sensing*, vol. 45, no. 11, pp. 3317–3341, Nov. 2007.

[16] T. Strozzi and U. Wegmuller, "Land subsidence in Mexico City mapped by ERS differential SAR interferometry," in *IEEE 1999 International Geoscience and Remote Sensing Symposium. IGARSS'99 (Cat. No. 99CH36293)*, vol. 4. IEEE, 1999, pp. 1940–1942.

[17] P. López-Quiroz, M.-P. Doin, F. Tupin, P. Briole, and J.-M. Nicolas, "Time series analysis of Mexico City subsidence constrained by radar interferometry," *Journal of Applied Geophysics*, vol. 69, no. 1, pp. 1–15, 2009.

[18] B. Osmanoğlu, T. H. Dixon, S. Wdowinski, E. Cabral-Cano, and Y. Jiang, "Mexico City subsidence observed with persistent scatterer InSAR," *International Journal of Applied Earth Observation and Geoinformation*, vol. 13, no. 1, pp. 1–12, 2011.

[19] Y. Yan, M.-P. Doin, P. López-Quiroz, F. Tupin, B. Fruneau, V. Pinel, and E. Trouvé, "Mexico City subsidence measured by InSAR time series: Joint analysis using PS and SBAS approaches," *IEEE Journal of Selected Topics in Applied Earth Observations and Remote Sensing*, vol. 5, no. 4, pp. 1312–1326, 2012.

[20] G. F. Vega, "Subsidence of the city of Mexico: A historical review," in *Proceedings of the Anaheim Symposium*, no. 121, 1976, pp. 35–38.

[21] J. M. D. Blasco, "snap2stamps," [Accessed on 24/01/2025]. [Online]. Available: https://github.com/mdelgadoblasco/snap2stamps

[22] A. Hooper, "StaMPS," [Accessed on 24/01/2025]. [Online]. Available: https://github.com/dbekaert/StaMPS

[23] K. Hormann, "Barycentric interpolation," in *Approximation Theory XIV: San Antonio 2013*. Springer, 2014, pp. 197–218.

[24] C. B. Barber, D. P. Dobkin, and H. Huhdanpaa, "The quickhull algorithm for convex hulls," *ACM Transactions on Mathematical Software (TOMS)*, vol. 22, no. 4, pp. 469–483, 1996.

[25] J. C. Curlander and R. N. Mcdonough, *Synthetic Aperture Radar: Systems and Signal Processing*. Hoboken, NJ: John Wiley & Sons, 1991.

[26] N. Ustalli, M. N. Peixoto, T. Kraus, U. Steinbrecher, G. Krieger, and M. Villano, "Experimental demonstration of staggered ambiguous SAR mode for ship monitoring with TerraSAR-X," *IEEE Transactions on Geoscience and Remote Sensing*, vol. 61, pp. 1–16, 2023.

[27] N. Ustalli, M. Nogueira Peixoto, T. Kraus, U. Steinbrecher, G. Krieger, and M. Villano, "Experimental demonstration of ambiguous staggered SAR with waveform alternation for coastal surveillance," *IEEE Geoscience and Remote Sensing Letters*, vol. 21, pp. 1–5, 2024.